Eur. Phys. J. Plus (2025) 140:510
https://doi.org/10.1140/epjp/s13360-025-06448-0

THE EUROPEAN PHYSICAL JOURNAL PLUS

Regular Article

Investigation of structural, electronics, and optical characteristics of cubic $SrZr_{1-x}Ru_xO_3$ perovskites: first-principles study

Said M. Al Azar[1,a], Anas Y. Al-Reyahi[2], Ahmad A. Mousa[3], Saber Saad Essaoud[4,5], Riad S. Masharfe[1], Ibrahim Ghabar[1], Nabil Al-Aqtash[2], Mohammed Elamin Ketfi[6], Mohammed S. Abu-Jafar[7], Emad K. Jaradat[8], Watheq Al-Basheer[9], Ahmad Mufleh[10]

[1] Department of Physics, Faculty of Science, Zarqa University, Zarqa 13132, Jordan
[2] Department of Physics, Faculty of Science, The Hashemite University, P. O. Box 330127, Zarqa 13133, Jordan
[3] Department of Basic Sciences, Middle East University, Amman 11831, Jordan
[4] Department of Physics, University of M'sila, 28000 M'sila, Algeria
[5] Laboratoire de Physique des Particules et Physique Statistique, Ecole Normale Supérieure-Kouba, Vieux-Kouba, BP 92, 16050 Algiers, Algeria
[6] Department of Electronics, Faculty of Technology, University of M'sila, 28000 M'sila, Algeria
[7] Physics Department, An-Najah National University, Nablus, Palestine
[8] Department of Physics, Faculty of Science, Imam Mohammad Ibn Saud Islamic University, 11623 Riyadh, Saudi Arabia
[9] Department of Physics, King Fahd University of Petroleum and Minerals, 31261 Dhahran, Saudi Arabia
[10] Preparatory Deanship, Prince Sattam Bin Abdulaziz University, Al-Kharj, Saudi Arabia

Received: 16 February 2025 / Accepted: 16 May 2025

Abstract This work addresses the effect of substituting Zr atoms with Ru atoms at different concentrations in perovskite $SrZrO_3$ on the widening of the band gap and the change in the electronic and magnetic states of the material. Density functional theory (DFT) based on the all-electron full-potential linearized augmented plane-wave method was used for the calculations. The results obtained for the energy gap show that their values gradually decreased from 4.20 eV in the parent $SrZrO_3$ to zero with 50% Zr substitution by Ru, accompanied by a linear decrease in the lattice constant from 4.177 to 4.085 Å. This trend is consistent with Vegard's law. The introduction of Ru induces a ferromagnetic state, with the total magnetic moment reaching 1.25 μB at a concentration of $x = 0.5$. The $SrZr_{1-x}Ru_xO_3$ series compounds showed good thermal properties, as their coefficient of thermal expansion is low, and their lattice thermal conductivity does not exceed 4.0 W m^{-1} K^{-1} at room temperature, and under pressure reached 30 GPa. The involvement of the oxygen $2p$ states with the $4d-t_{2g}$ states of both ruthenium and zirconium is critical in the optical transitions observed in $SrZr_{1-x}Ru_xO_3$ compounds. These findings demonstrate that Ru-doped $SrZrO_3$ is a promising candidate for spintronics, photovoltaics, and sustainable energy technologies due to its tunable band gap, robust magnetism, and exceptional thermal stability.

1 Introduction

Strontium zirconate ($SrZrO_3$), a widely studied perovskite, has applications in electrical ceramics, refractories, thermal coatings, and catalysis. It serves as a high-temperature proton conductor in fuel cells and H_2 sensors [1]. This insulator has a wide band gap, high hardness, stiffness, and melting point [2]. Kennedy and his coworkers investigated experimentally the high-temperature phase transitions in $SrZrO_3$. They revealed that the transition from $I4/mcm$ ($a^\circ a^\circ c$) to $Pm\bar{3}m$ ($a^\circ a^\circ a^\circ$) is allowed to be continuous, i.e., it is a first-order transition as in Landau theory [3, 4]. Likewise, examination of the powder neutron diffraction data confirmed the following sequence of phase transitions with Glazer notations for octahedral tilting: orthorhombic ($Pnma$) (a^+bb) → orthorhombic ($Cmcm$) ($a^\circ b^+c$) → tetragonal ($I4/mcm$) ($a^\circ a^\circ c$) → cubic ($Pm\bar{3}m$) ($a^\circ a^\circ a^\circ$). The diffraction patterns when heating from 1373 to 1423 K do not present evidence of any superlattice reflections. So, the structure is cubic with a space group ($Pm\bar{3}m$). Furthermore, because of its very high melting temperature (~2920 K), most of its applications execute in the cubic phase [5]. Notably, studies on $AgMgF_3$ and $KMgF_3$ have demonstrated their potential as capacitor materials in electrical equipment, as calculations of effective born charges revealed enhanced dielectric polarization effects [6]. Furthermore, double perovskites demonstrate unique functional characteristics [7, 8].

Doped $SrZrO_3$ (with Al, Sc, Y, etc.) enhances protonic conductivity for hydrogen sensors and fuel cells [9–13]. DFT studies show In, Yb, and Y improve protonic conductivity in $SrZrO_3$ [11], while Rh doping reduces it [12]. In 2010, Ito et al. received the US patent for synthesizing a single phase of $SrZr_{1-x}Ru_xO_3$ where ($x = 0.05$, 0.10, and0.15) to use as proton conductors in the electrochemical cell [14]. There are no detailed theoretical or experimental studies for Ru-doped $SrZrO_3$ perovskite, although

[a] e-mail: Salazar@zu.edu.jo (corresponding author)

Published online: 10 June 2025

Ruocco et al. recently synthesized $SrZr_{0.88729}Ru_{0.11271}O_3$ catalyst using the auto-combustion method. The results show that it has high reducibility, main specific surface area, and good resistance to thermal stresses in terms of conversion and stability during a long duration. Thus, it performs well in methane dry reforming [15, 16]. In the present article, $SrZr_{1-x}Ru_xO_3$ ceramics at $x = 0$, 0.125, 0.25, 0.375, and 0.5 were investigated using the DFT method, where their structural, electronic, magnetic, and optical properties were predicted.

Transition metal (TM) doping tunes electronic properties, enabling optical/optoelectronic applications. Intermediate band (IB) materials with transition metals have been used as solar cell candidates to increase efficiency over the Shockley–Queisser limit [17]. Furthermore, diluted magnetic semiconductor (DMS) could be occurring as a result of itinerant carriers and local transition metal magnetic moment. The maximum red emission from $SrZr_{1-x}Mn_xO_3$ takes place at $x \sim 0.001$ according to Cho and Lee [18]. $SrZrO_3:Eu^{3+}$ exhibits luminescence [19–21]. Nb-doped $SrTiO_3$ is used in solid oxide fuel cells and nonvolatile memories. Furthermore, donor-doped $SrTiO_3$ is used in sensors, varistors, grain boundary layer capacitors, and catalysts [22]. Gillani et al. [5, 23] studied the structural stability and the improvement in electronic and optical features of doped $SrZrO_3$ using the DFT method. Furthermore, they investigated the magnesium doping effect on the band gap and optical properties of $SrZrO_3$. Park et al. [24] investigated the current–voltage characteristics of Cr-doped $SrZrO_3$ film grown on $SrRuO_3/SrTiO_3$ superlattice using off-axis radio-frequency sputtering. They suggested the mechanism of resistive switching. Weston et al. investigated computationally the $SrZrO_3$ band gap engineering by doping Ti. Also, they demonstrated that an effective 1×1 $SrTiO_3/SrZrO_3$ superlattice along the [001] direction leads to enhancing carrier mobility [25]. Furthermore, several studies explore advanced energy storage and harvesting technologies, including light-driven supercapacitors [26], wearable fabric-based supercapacitors [27], Mn-doped ZnO/rGO electrodes [28], LDPE-derived graphene for triboelectric nanogenerators, thermoelectric supercapacitors [29], and PVDF-PZT composites for self-charging supercapacitors [30], highlighting their synthesis, characterization, and future applications in wearable sensors and sustainable energy systems [31].

We note that there is a lack of investigations that have been executed on the bulk properties of various levels of concentration of Ru-doped on $SrZrO_3$ at high-temperature phases at ambient conditions. Therefore, this paper aims to bridge this knowledge gap by offering detailed theoretical calculations and providing reasonable physical interpretations of the results that can aid future experimental and application-based works in this field. The study's novelty is centered on the ability to modify the material phase and the band gap by varying the dopant concentration. The parent material, $SrZrO_3$, has been transformed from an insulator to a ferromagnetic half-metal and finally into a ferromagnetic metal by altering the concentration of Ru doped. However, the search results do not provide specific information on the concentration of Ru needed to achieve each phase transition.

The article is organized as follows: After introduction, Sect. 2 presents the technical details of computational methods. Section 3 is devoted to the results and discussion, including structural and dynamic stability, electronic and magnetic, optical, and thermoelectric properties, and the previously available theoretical and experimental data. Finally, we summarize our main results in Sect. 4.

2 Computational methods

In this article, the density functional theory (DFT) [32, 33] calculations are carried out using the all-electron full-potential linearized augmented plane-wave (FP-LAPW) method as implemented in the WIEN2k program [34]. The Kohn–Sham equation i.e., non-interacting one-electron Schrödinger equation,

$$\left(-\frac{1}{2}\nabla_i^2 + V_{\text{eff}}(\boldsymbol{r}) - \epsilon_i\right)\psi_i(\boldsymbol{r}) = 0, \tag{1}$$

should be solved self-consistently with charge density $n(\boldsymbol{r})$ because effective potential $V_{\text{eff}}(\boldsymbol{r})$ depends on $n(\boldsymbol{r})$. Slater's muffin-tin (MT) spheres model is employed to divide the cell into two zones. All quantities around the atoms are expanded in spherical harmonics, whereas in the interstitial they are treated as plane waves. The computed electronic, structural, optical, and transition parameters are performed using general gradient approximation as parameterized in Perdew–Burke–Ernzerhof (PBE-GGA) to incorporate the exchange–correlation potential functional.

The cubic $SrZrO_3$ perovskite unit cell structure has Sr at 1a(0,0,0) Wyckoff position, Zr at 1b(1/2,1/2,1/2) position, and O at 3c(0,1/2,1/2), (1/2,0,1/2), (1/2,1/2,0) positions. Each Zr atom is bonded to six O atoms as the nearest neighbors to form ZrO_6 octahedra, while the O atom is bonded to four Sr and two Zr neighbors, whereas the Sr atom is bonded to 12 O atoms as the nearest neighbors to form SrO_{12} cuboctahedra. All Sr–O bond lengths are ~ 2.97 Å and it is an ionic, while all Zr–O bond lengths are ~ 2.10 Å and it is covalent. The corner-sharing octahedral tilt angles are 0°.

In doped $SrZrO_3$, Zr-atoms are partially replaced by Ru-atoms. The supercell approach is significant to conquering the boundaries effect in studying doped $SrZrO_3$. The simulation is carried out on a $(2 \times 2 \times 2)$ supercell of cubic $SrZr_{1-x}Ru_xO_3$ perovskite as shown in Fig. 1, for $x = 25\%$. For all calculations, the atom's electronic configurations are divided into core and valence electrons. Here, we treated the Sr $4s^24p^65s^2$, Zr $4s^24p^64d^25s^2$, Ru $4d^75s^1$, and O $2s^22p^4$ electrons as valence electrons. Moreover, the muffin-tin radii are chosen to be 1.9, 1.8, 1.77, and 1.63 a.u for Sr, Zr, Ru, and O, respectively. The $l_{\max} = 10$ is used for the wave function expansion inside the muffin-tin spheres, whereas the charge density is expanded in the Fourier series truncated at $G_{\max} = 16(a.u)^{-1}$. In the interstitial region, the single electron wave functions were expanded using plane-wave basis set with

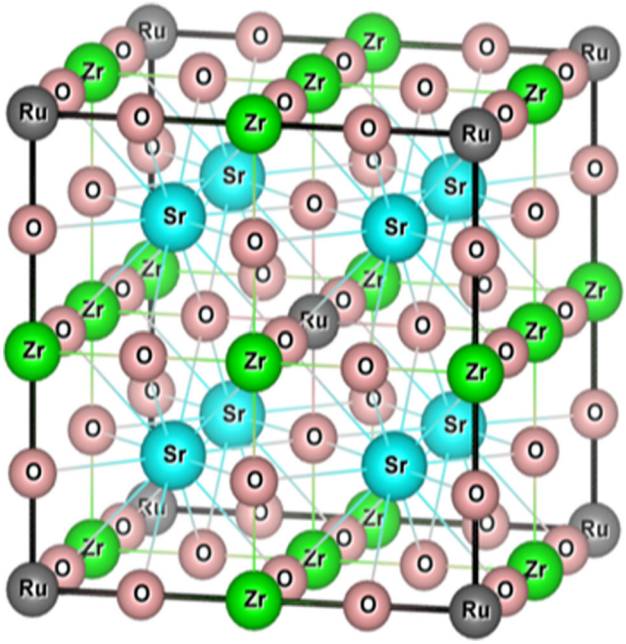

Fig. 1 ($2 \times 2 \times 2$) supercell of cubic $SrZr_{1-x}Ru_xO_3$ perovskite at $x = 0.25$ (using XcrysDen program [35])

cutoff parameter $K_{\max} \times R_{\mathrm{MT}} = 8$, where R_{MT} is the smallest muffin-tin radii and $K_{\max}$ represents the largest K-vector value in irreducible Brillion zone (IBZ).

The GIBBS2 program employs static total energy $E(V)$ and phonon frequencies or phonon density of states obtained from ab initio calculations to determine thermodynamic properties [36]. GIBBS2 utilizes four models: Debye–Slater, Debye–Gruneisen, Debye–Einstein, and the full quasi-harmonic approximation (QHA), to enhance the complexity and accuracy of the results.

3 Results and discussion

3.1 Structural and dynamical stability

The unit cell of each perovskite of $SrZr_{1-x}Ru_xO_3$ ($x = 0$, 0.125, 0.25, 0.375, and 0.5) is optimized to investigate the lattice constant (a_0) and ground state energy (E_0) by fitting the Birch–Murnaghan equation of state [37]. The results of this optimization have been compared with previous findings and are tabulated in Table 1. It is obvious from the table that the optimized DFT lattice parameters of Ru-doped $SrZrO_3$ perovskites are in the range of 4.085–4.177 Å. This result of lattice constants is consistent with Vegard's law where a_0 decreases with increasing the Ru concentration because the size of the Ru ion is smaller than the Zr ion. The calculated a_0 of $SrZrO_3$ (4.177 Å) without including the effect of thermal expansion is greater than the previous experimental value (4.154 Å) by 0.55%. In addition, the bulk modulus (B) is in the range 151.8–156.3 GPa; it increases with increases in the Ru %. Some previous data for $SrRuO_3$ are included in Table 1 for comparison. Goldschmidt tolerance factor (t) [38] is defined by

$$t = \frac{r_A + r_O}{\sqrt{2}(r_B + r_O)} \tag{2}$$

where r_A and r_B are A and B cations' average ionic radii; r_o is the O anion's average ionic radii; and the octahedral factor ($\mu = r_B/r_O$) [39] is used to evaluate the crystallography stability and structural distortion of the perovskites. The t values range from 0.947 to 0.970 indicating the cubic perovskite structure [40]. To calculate the tolerance factor at different Ru concentrations, we use the average ionic radius at B cation by the expression $r_B = (1-x)r_{Zr} + xr_{Ru}$, where x is the Ru % in the compounds. We used $r_{Sr} = 1.44$ Å for Sr^{+2}, $r_{Zr} = 0.72$ Å for Zr^{+4}, $r_{Ru} = 0.62$ Å for Ru^{+4}, and $r_O = 1.40$ Å for O^{-2} as in Shannon ionic radii [41]. The octahedral factors have been calculated, and their values ranged from 0.478 to 0.514, which are greater than 0.425 (the lowest limit of μ for perovskite formability) (see Figure S1). Figure 2 shows the energy difference from the structure ground state energy as a function of the lattice parameter for $SrZr_{1-x}Ru_xO_3$, where $x = 0.0$, 0.125, 0.25, 0.375, and 0.5. Notably, the lattice parameter decreases with increasing Ru concentration, indicating a contraction of the crystal structure with higher Ru substitution. Furthermore, the optimized lattice parameters range from 4.082 to 4.177 Å as derived from the curve fitting. The ΔE values span from approximately 0.5–1.5 eV, with the minima becoming shallower at higher$x$, suggesting reduced structural stability with Ru doping. The x-axis ranges from 3.95 to 4.3 Å, covering the relevant structural variations.

Table 1 Lattice parameters, bulk modulus, optimized energy, and the tolerance factor of $SrZr_{1-x}Ru_xO_3$ comparison with previous studies

Structure	Functional	a (Å)	B (GPa)	E_0 (Ry)	t	References
$SrZrO_3$	GGA-PBE	4.177	151.8	− 14,010.44244	0.947	This work
	GGA-PBE	4.186	163			[42]
	LDA	4.095	171			[43]
	Exp	4.154	150			[4]
$SrZr_{0.875}Ru_{0.125}O_3$	GGA-PBE	4.152	153.7	− 14,243.533988	0.953	This work
$SrZr_{0.75}Ru_{0.25}O_3$	GGA-PBE	4.126	155.5	− 14,476.62398	0.959	
$SrZr_{0.625}Ru_{0.375}O_3$	GGA-PBE	4.107	156.3	− 14,709.709038	0.964	
$SrZr_{0.5}Ru_{0.5}O_3$	GGA-PBE	4.082	155.0	− 14,942.80230	0.970	
$SrRuO_3$		3.92 3.93^{exp} 3.94 4.04		− 15,865.004989	0.994 0.95	[44]

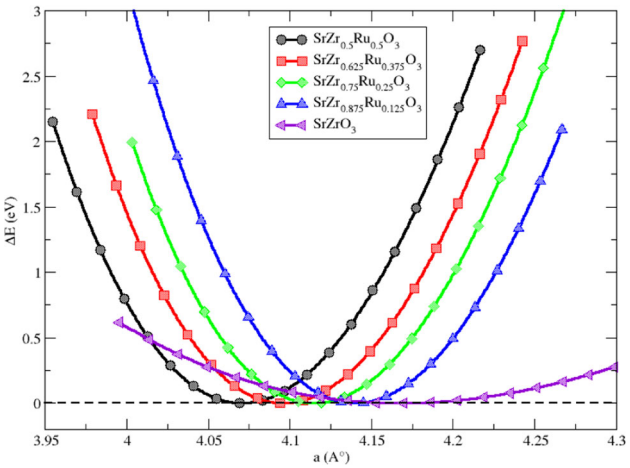

Fig. 2 Optimized lattice parameters of $SrZr_{1-x}Ru_xO_3$, where $x = 0.0, 0.125, 0.25, 0.375$, and 0.5 versus ΔE (ΔE represents the energy difference from the structure ground state energy)

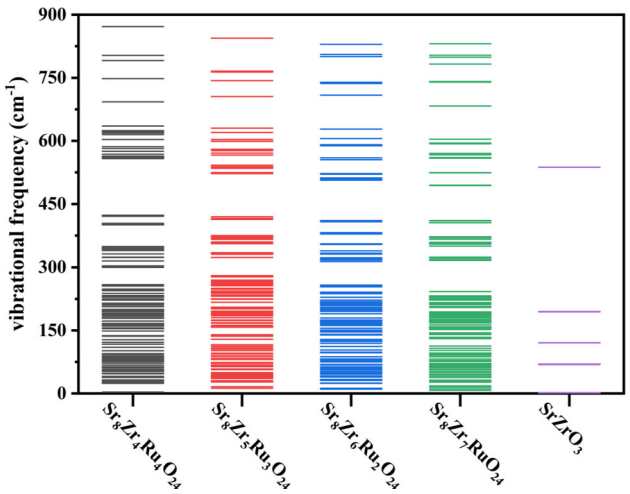

Fig. 3 Vibrational frequencies ($3N - 6$) of the lowest-energy structures of $SrZr_{1-x}Ru_xO_3$ compounds series with $x = 0$, 0.125, 0.25, 0.375, and 0.5

Finally, we used a finite differences method to calculate the phonon frequency modes at the Γ-point to investigate the dynamic stability. It is discovered that all of the lowest energy of $SrZr_{1-x}Ru_xO_3$ structures, as depicted in Fig. 3, have positive vibrational frequencies devoid of imaginary components; as a result, every structure has a real local minimum. Regarding the potential for these compounds to form at varying temperatures, phonon simulations need to account for the impacts of heat on dynamical stability.

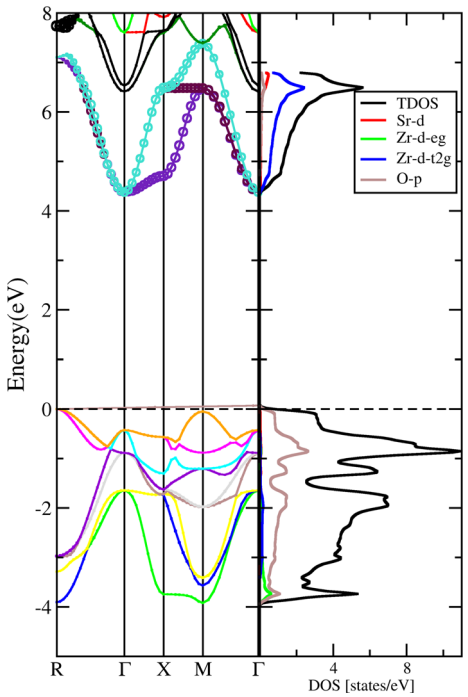

Fig. 4 Band structure and TDOS with ℓ-components PDOS of $SrZrO_3$ by utilizing the mBJ method

Table 2 VBM, CBM, and band gap energy of $SrZr_{1-x}Ru_xO_3$ at different x values

Structure	$SrZrO_3$	$SrZr_{0.875}Ru_{0.125}O_3$	$SrZr_{0.75}Ru_{0.25}O_3$	$SrZr_{0.625}Ru_{0.375}O_3$	$SrZr_{0.5}Ru_{0.5}O_3$
VBM	− 0.0546	− 0.83395	− 0.81918	− 0.34747	
CBM	3.32566	1.69157	1.75252	1.65059	
E_g	4.20 (mBJ) 3.38 (PBE) 3.42[a],3.37[b] 3.2[c] 5.6[d], 5.2[e]	2.56 (PBE)	2.57(PBE)	1.998(PBE)	0
Direction	R-Γ	X-Γ	X-Γ	Γ-Γ	-

[a]GGA, FP-LAPW Ref. [42]
[b]LDA, pseudopotential Ref. [43]
[c]PBEsol, FP-LAPW Ref. [46]
[d]Exp. Ref. [47]
[e]Exp. Ref. [48]

3.2 Electronic and magnetic properties

In this subsection, the band structure and density of states of ordered cubic $2 \times 2 \times 2$ supercell $SrZr_{1-x}Ru_xO_3$ structures with $x = 0$, 0.125, 0.25, 0.375, and 0.5 are presented and interpreted. Furthermore, the magnetic characteristics of $SrZr_{1-x}Ru_xO_3$ are extracted from the electronic structure.

Figure 4 shows the band structure and DOS of cubic $SrZrO_3$ perovskite. The obtained band structure and DOS of $SrZrO_3$ agree with the previous calculations [42, 43, 45]. It has an indirect wide band gap (R→Γ) with a value equal to 4.20 (3.38) eV using mBJ (PBE) parameterization. This result is consistent with the previous theoretical finding of 3.42 eV (PBE parameterization) and underestimates the experimental value 5.6 eV for the indirect gap as in reference [42] by approximately 25%. The upper valence band of $SrZrO_3$ is wide and equal to 4.30 eV. It has the valence band maximum (VBM) at the R symmetry point. It is mainly an O $2p$ electronic character with a mixture of σ*-bands and narrow π*-bands. Otherwise, the antibonding (π* and σ*) in the lower conduction bands is formed mainly from Zr $4d$ states hybridized with O $2p$ states. The Zr $4d-t_{2g}$ (π*-triplet) states are next to the gap, and they are mixed with Sr $5s$ while Zr $4d-$eg (σ*-doublet) states located up in the energy range 8.1–12.5 eV (does not shown here). The conduction band minimum (CBM) is at Γ point. Also, the width of π* conduction bands is 3.40 eV. The nine valence bands at the center of BZ (Γ-point) have threefold degeneracy (Γ_{15} and Γ_{25}) which are apart by energies 0.78 and 0.7 eV.

Figure 5 displays the spin-polarized band structure for $SrZr_{1-x}Ru_xO_3$ at different Ru dopant concentrations. It is clear that at ($x = 0.5$) Ru concentration, the band gap is collapsed although it has quasi-flat bands near the Fermi level. The lower conduction bands in the spin-up channel crossover the E_F. Therefore, its behavior is metallic. The other three concentrations 0.125, 0.25, and 0.375 of Ru still have band gaps in the spin-up channel. The formed band gaps decrease with increasing the Ru concentration as tabulated in Table 2. Furthermore, the band gap at ($x = 0.125$) and ($x = 0.25$) Ru concentrations stays an indirect gap as in $SrZrO_3$, whereas it turns to a direct one at ($x = 0.375$).

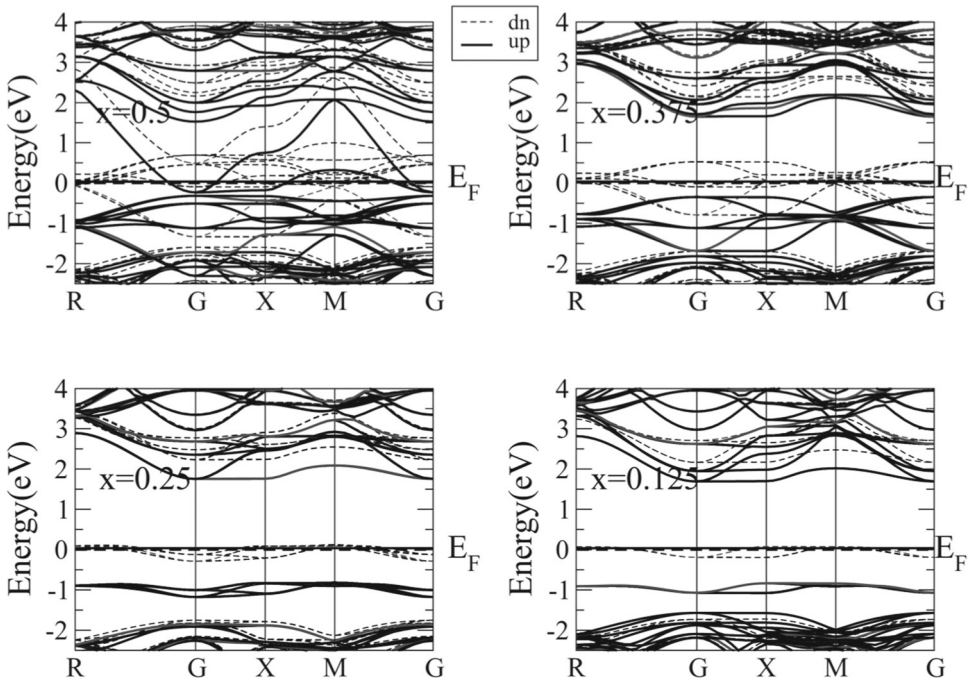

Fig. 5 Spin-polarized band structure for $SrZr_{1-x}Ru_xO_3$

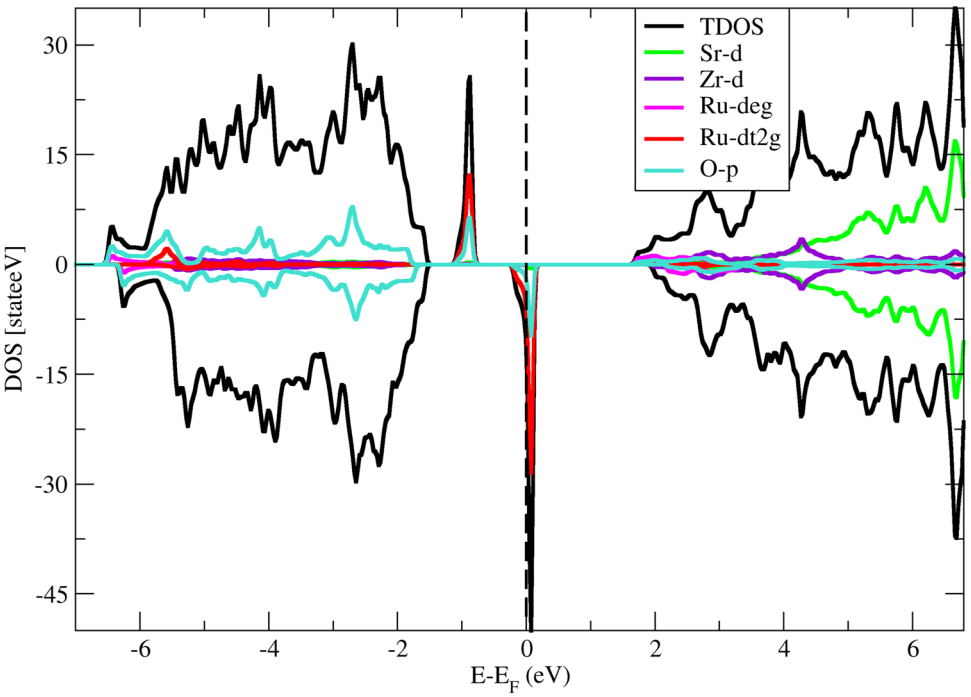

Fig. 6 Total and the ℓ-components partial DOS of $SrZr_{0.875}Ru_{0.125}O_3$

To analyze and interpret what occurs when Ru ions are added to $SrZrO_3$ the ℓ-components partial DOS should be drawn. Figure 6 displays the total and ℓ-components resolved DOS for $SrZr_{0.875}Ru_{0.125}O_3$. The DOSs of the other concentrations are displayed in Figures S2, S3, S4, and S5 in the supplementary data. At Ru $x = 0.125$ concentration, the electronic structure of $SrZrO_3$ transitions from insulator to half-metal with a band gap at the spin-up channel. As a succession, the TDOS for $x = 0.25$ and 0.375 also shows a band gap in the spin-up channel, whereas there is no gap at $x = 0.5$ (see Figure S6 in the supplementary data). The spin-up channel's narrow peak in the valance band near the Fermi level at $E = -1.0$eV is formed from the hybridization between Ru ($d-t_{2g}$) and O (2p) orbitals. In contrast, the peak in spin-down crosses the Fermi level (see Figure S4 in the supplementary data).

The bandgaps in the spin-up channel as a function of Ru concentration change in a unique way from 4.2 (3.38) eV by using mBJ (PBE) to 0 eV). Table 2 tabulates the VBM, CBM, and band gaps of studied materials. They mostly decrease with increasing the Ru concentration to reach zero bandgap at $x = 0.5$, metallic behavior of $SrZr_{0.5}Ru_{0.5}O_3$. In addition, they change from indirect at

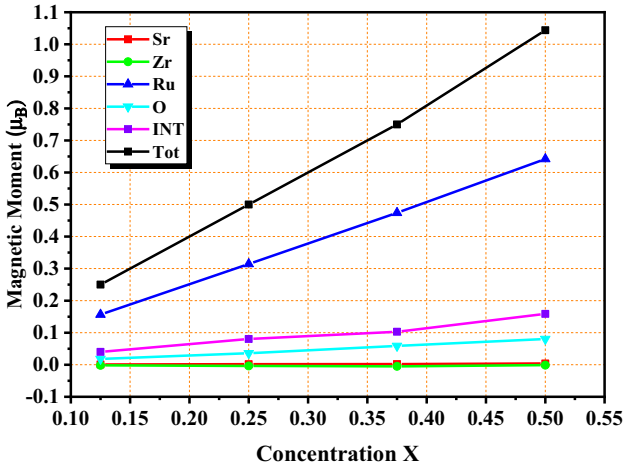

Fig. 7 Total and atom resolved spin magnetic moment of $SrZr_{1-x}Ru_xO_3$ normalized to one-unit cell at different x values

the parent to direct at $x = 0.375$. The insulator-to-half-metal transition takes place at about $x = 0.125$ Ru concentration, whereas the half-metal-to-ferromagnetic metal transition is near a 50% Ru concentration ($x = 0.5$).

The total magnetic moment of the compound $SrZr_{1-x}Ru_xO_3$ at different x values, as well as the contributions of the atoms to this magnetic moment, was calculated, and its changes were plotted as a function of concentration in Fig. 7. From this figure, a linear increase in the total magnetic moment appears with the increase in the concentration of Ru atoms. From the analysis of the curves of the magnetic moments of the atoms forming the compound, the Ru atoms revealed their dominant contribution to this magnetic moment, unlike the rest of the atoms, which had modest contributions. Table S1 presents the total spin magnetic moments M_{tot} and atom-resolved spin magnetic moment for $SrZr_{1-x}Ru_xO_3$ where $x = 0$, 0.125, 0.25, 0.375, and 0.5. We notice that the total spin magnetic moment increases with increasing the Ru doping concentration. It changes from zero in the parent $SrZrO_3$ (insulator) to 8.35 μ_B (ferromagnetic material) at the supercell when 50% of Zr is replaced by Ru. For the doped compounds, the Ru atoms have the most contribution in the spin magnetic moment ~ 1.25 μ_B. The interstitial contribution varies from 0.3 to 1.27 μ_B when Ru % increases. Also, the very weak interaction between Ru and Zr is in the opposite direction. For alloys with Ru concentration from $x = 0.125$ to $x = 0.375$, the total spin magnetic moments are following the Pauling–Slater curve. This trend makes these materials characterized as ferromagnetic half-metal materials. On the other hand, the $SrZr_{0.5}Ru_{0.5}O_3$ is categorized as a ferromagnetic material.

3.3 Optical properties

In this subsection, the optical response in the core-level spectra of $SrZrO_3$ and Ru-doped $SrZrO_3$ perovskites is calculated in the photon energy range 0–14 eV by using the FP-LAPW method with PBE-GGA exchange–correlation functional. The details about computing optical response functions and the matrix elements as implemented in the LAPW method can be found in Ambrosch–Draxl and Sofo's work and reference within [49]. Furthermore, using the calculated band structure together with the density of states we have analyzed the interband contribution to the optical properties of cubic $SrZr_{1-x}Ru_xO_3$. Optical conductivity is equivalent to absorption and delivers information on how external parameters concern the electronic configuration.

Figure 8 shows the real and imaginary dielectric constant for $SrZr_{1-x}Ru_xO_3$ as a function of photon energy. The comparison between $SrZrO_3$ and Sr(Zr, Ru)O_3 in dielectric constant shows that there is a difference in optical response. The nonmetal behavior in $SrZrO_3$ is clear, but in Sr(Zr, Ru)O_3 its behavior changes to metal. From the real dielectric plot, all curves of $SrZrO_3$:Ru have four roots, except that $SrZr_{0.825}Ru_{0.125}O_3$ has three roots on the photon energy axis ($\varepsilon_1 = 0$). These roots indicate that there is no response to incident light at these energy values due to the plasmon oscillation.

Figure 9 shows the optical properties of $SrZrO_3$. The static dielectric function $\varepsilon(0)$ equals 4.0 compared to the previous results (4.6) as in reference [46]; also the static real refractive index $n(0)$ equals 2.0 ($n(0) = 2.2$ in ref. [46]). In the transparency region, n increases with energy and reaches the peak ($n = 2.55$) at $E = 4.1$eV (ultraviolet region), whereas at high ultraviolet ($E > 6.0$eV) the refractive index decreases rapidly to attain 0.25 at $E = 14.0$eV. The imaginary (absorptive) dielectric part shows three structure profiles. The first maximum peak of ε_1 is at ~ 6.2 eV which reveals the UV harvesting capacity. Also, the absorption threshold energy reaches 4.0 eV. The first peak of absorption coefficient is at energy 6.2 eV with $\alpha \sim 1.25 \times 10^6 \text{cm}^{-1}$ due to direct gap and high DOS. This value is very high compared to the conventional absorbed materials. The reflectivity R in the visible light region is about 10% only, and the absorption coefficient is almost zero which indicates that the material is transparent.

In Fig. 10, the optical properties of $SrZr_{0.5}Ru_{0.5}O_3$ are depicted. The dielectric constant ε at low energy (far infrared region) tends to infinity, and its behavior becomes similar to the metals with high reflectivity of ~ 100% at the far-infrared region. Optical energy loss is the main factor determining the reliability of optoelectronic devices. As shown in Fig. 9, the photon energy loss of $SrZr_{0.5}Ru_{0.5}O_3$ is minimal in the energy range from 0 to 4 eV (infrared and visible spectra). A further increase in incident photon

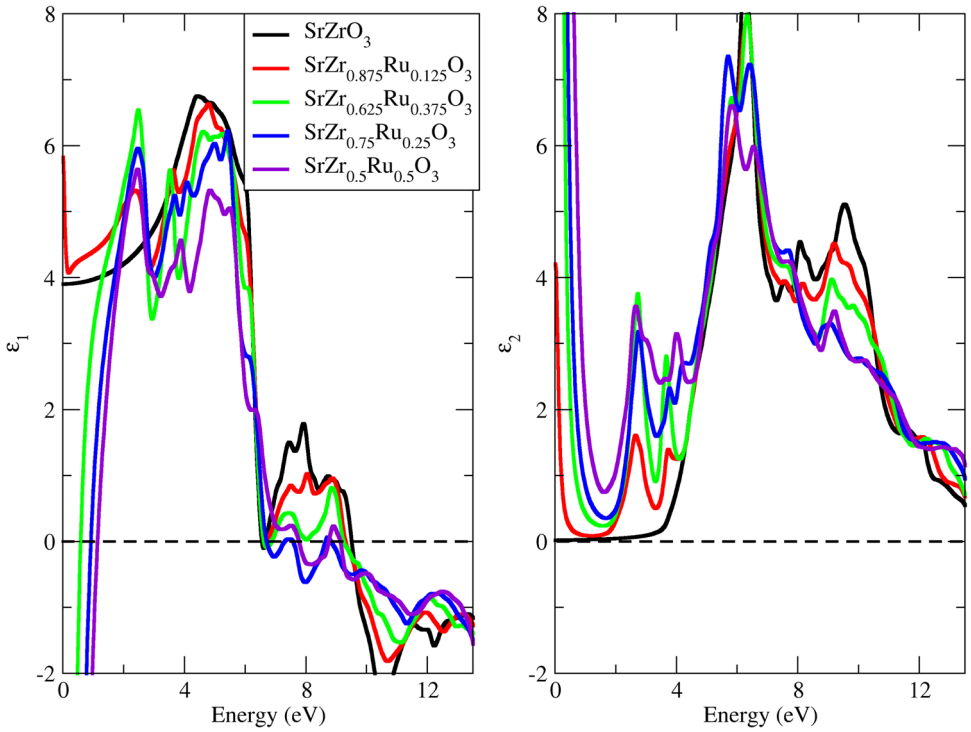

Fig. 8 Real and imaginary dielectric constant for $SrZr_{1-x}Ru_xO_3$ as a function of energy

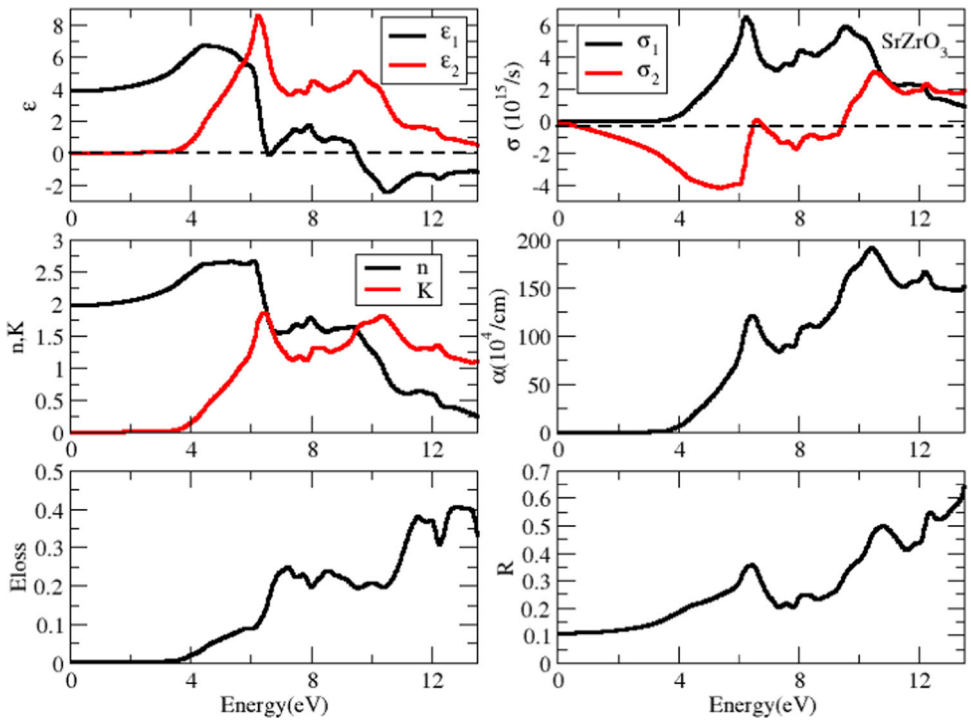

Fig. 9 $SrZrO_3$ optical properties

energy would increase optical loss. The peak at ~ 1.0 eV in loss function refers to the plasma resonance-related characteristics. The identification of a material as an insulator or conductor is based on the value of $\varepsilon_1(\omega)$ below and above plasma frequency ω_p. Insulators have values of $\varepsilon_1(\omega)>0$, whereas conductors have values of $\varepsilon_1(\omega)<0$ [50]. The same analysis is for Figures S7, S8, and S9 in the supplementary data. The figures demonstrate a Ru concentration-dependent insulating phase, with the energy range of insulating behavior progressively narrowing as doping increases: 0–9.0 eV (12.5% Ru), 0.5–9.0 eV (25% Ru), 1.0–7.7 eV (37.5% Ru), and 1.5–7.0 eV (50% Ru). At 0% Ru, the material remains insulating over all energies.

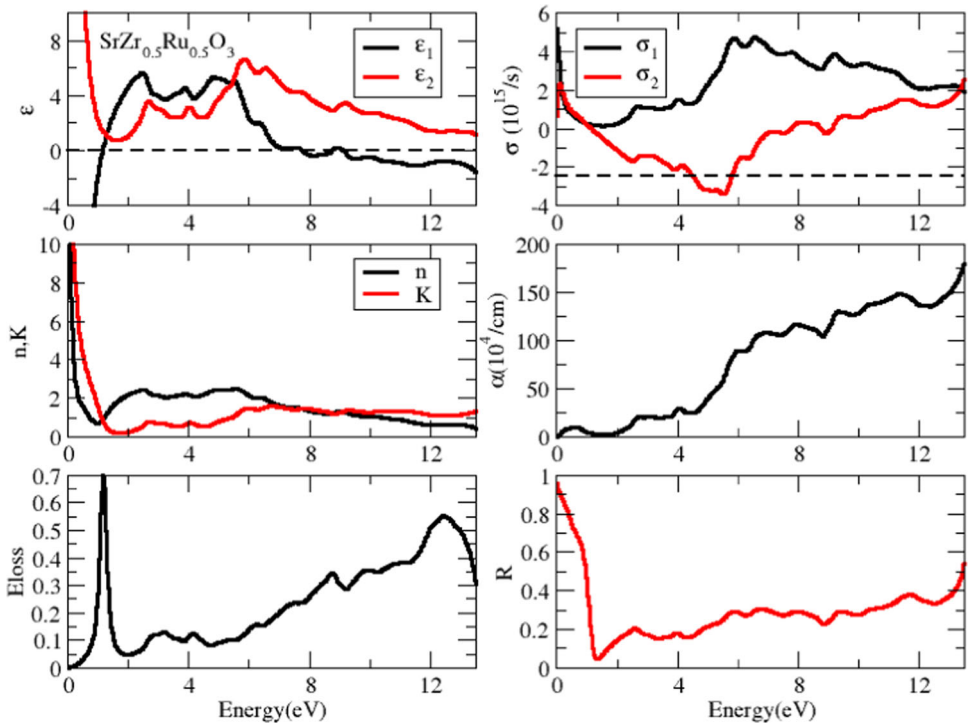

Fig. 10 Optical properties of $SrZr_{0.5}Ru_{0.5}O_3$

For doped compounds after $x = 0.125$ $\sigma(\omega)$ below 1.0 eV have zero-frequency spectral weights, which increase with the increasing of Ru concentration. The $2p$ O state and the $4d-t_{2g}$ states of both Ru and Zr play the main role in the optical transitions of $SrZr_{1-x}Ru_xO_3$ perovskites consistent with the conclusion in reference [51].

3.4 Thermodynamic properties

Within this subsection, we delved into the alterations in thermodynamic properties as they relate to temperature, spanning from 0 to 1500 K, and pressure, ranging from 0 to 30 GPa, on cubic $SrZr_{1-x}Ru_xO_3$, where x takes on values of 0, 0.125, 0.25, 0.375, and 0.5. Comprehensive underlying concepts and principles governing the thermodynamic properties have been discussed in reference [6] and the references cited within it.

Figure 11 displays a chart showing the lattice thermal conductivity (K_l) and isochoric heat capacity (C_V) of $ZrSr_{1-x}Ru_xO_3$ at various pressures and temperatures. The Slack model formula, as given by $K_l = \frac{A\theta_D{}^3 V^{1/3} m}{\gamma^2 n^{2/3} T}$, provides a means to calculate the thermal conductivity (K_l) [8]. Here, various components and parameters involved in the formula are defined as follows: where A is a physical constant with a specific value, which is determined by the expression $A = \frac{2.4310^{-8}}{1-\frac{0.514}{\gamma}+\frac{0.228}{\gamma^2}}$, θ_D represents the Debye temperature, γ stands for the Grüneisen parameter, V is the volume per atom in the material, n denotes the number of atoms present in the primitive unit cell, m represents the average mass of all the atoms within the crystal. It provides insight into the material's thermal transport characteristics. A discernible trend emerges from these data: As the temperature rises under all applied pressures, the K_l consistently decreases. This trend indicates that as the material's temperature increases, its ability to conduct heat through the lattice diminishes. In contrast, C_V exponentially increases as temperature rises, particularly at lower temperature ranges (0–300 K). Above 300 K, there is a sluggish increase in C_V. As the temperature surpasses Debye temperature, it aligns with Dulong–Petit limits ($C_v = 3NR$) [52]. This result dovetails with the experimental results of Ligny and Richet as reported in reference [53]. Furthermore, the values of K_l at a specific temperature increase as pressure increases, whereas C_v decreases as pressure increases.

While the entropy (S) provides an insight into system thermal energy, the thermal expansion (α) indicates the degree of tendency of the materials to expand when heated. As illustrated in Fig. 12, our observations reveal significant trends in the behavior of thermal expansion (α) and entropy (S) within the $ZrSr_{1-x}Ru_xO_3$ material under varying levels of applied pressure and temperature. When temperature is raised, both thermal expansion and entropy exhibit a conspicuous increase due to an increase in thermal vibrations. This indicates that as the material experiences higher temperatures, it becomes more prone to thermal expansion, and its entropy content also rises.

Conversely, when we examine α and S at a specific temperature point, we observe a contrasting pattern. As the applied pressure intensifies, both α and S are showing a discernible decrease because the vibrations tend to seize. This suggests that elevated pressure levels at a fixed temperature reduce the material's propensity for thermal expansion, leading to a decrease in its entropy content.

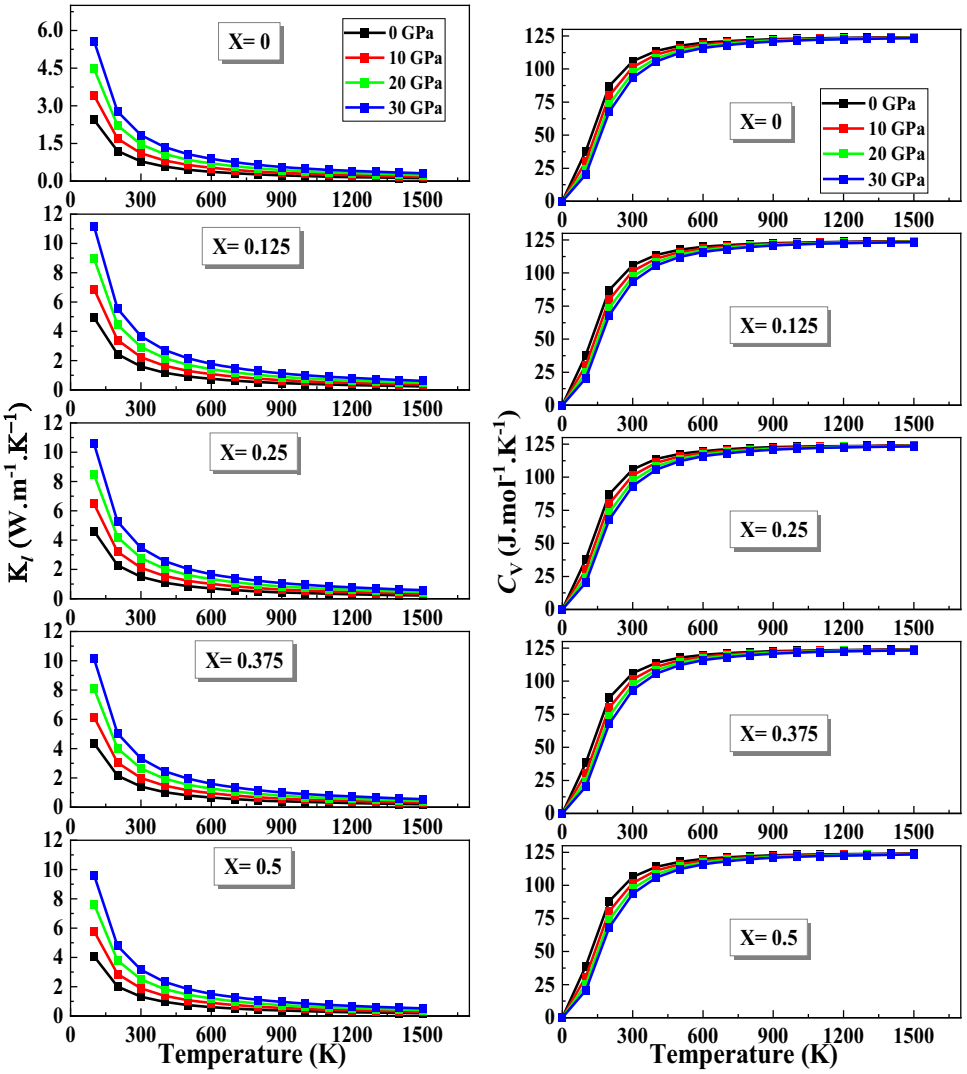

Fig. 11 Temperature dependence of the isochoric heat capacity (C_V) and the crystal lattice thermal conductivity (K_l) of $ZrSr_{1-x}Ru_xO_3$ at applied fixed hydrostatic pressures of 0, 10, 20, and 30 GPa

To summarize, Fig. 12 provides insights into how the thermal expansion and entropy properties of $ZrSr_{1-x}Ru_xO_3$ respond to changes in both temperature and pressure, highlighting their intricate relationship and influence on the material's behavior.

Table 3 provides essential thermodynamic and thermal properties of $ZrSr_{1-x}Ru_xO_3$ at standard conditions (0 GPa and 300 K). Isochoric heat capacity (C_v) and equilibrium entropy (S) increase with higher Ru concentration, indicating that as more ruthenium is incorporated into the material, its heat capacity and entropy also rise. This suggests a greater ability to store heat energy and a more disorderly arrangement of particles. Gruneisen parameter (γ) and thermal expansion factor (α) also exhibit an increase with increasing Ru concentration. This implies that the material becomes more responsive to changes in temperature and pressure as the Ru content rises. Higher values of α suggest increased thermal expansion, while a larger γ indicates greater sensitivity to compression or expansion. In contrast, Debye temperature (θ_D) and lattice thermal conductivity (K_l) both decrease as the Ru concentration increases. A lower θ_D signifies a reduction in the characteristic temperature at which lattice vibrations contribute to heat capacity, while a drop in K_l indicates reduced heat conduction through the lattice. These trends suggest that the introduction of more ruthenium disrupts the lattice structure and diminishes thermal conductivity.

In summary, the data in Table 3 demonstrate that increasing the Ru concentration in $ZrSr_{1-x}Ru_xO_3$ leads to higher C_v, S, γ, and α, while simultaneously reducing θ_D and K_l. These findings are crucial for understanding how the material's properties are influenced by changes in its composition and have implications for its potential applications in various fields.

4 Conclusions

The effects of Ru-doped $SrZrO_3$ cubic perovskites are investigated in the framework of density functional theory in the FP-LAPW approximation with GGA-PBE parameterization. Our key findings reveal: (1) For the Sr(Zr, Ru)O_3 ordered alloys, the lattice

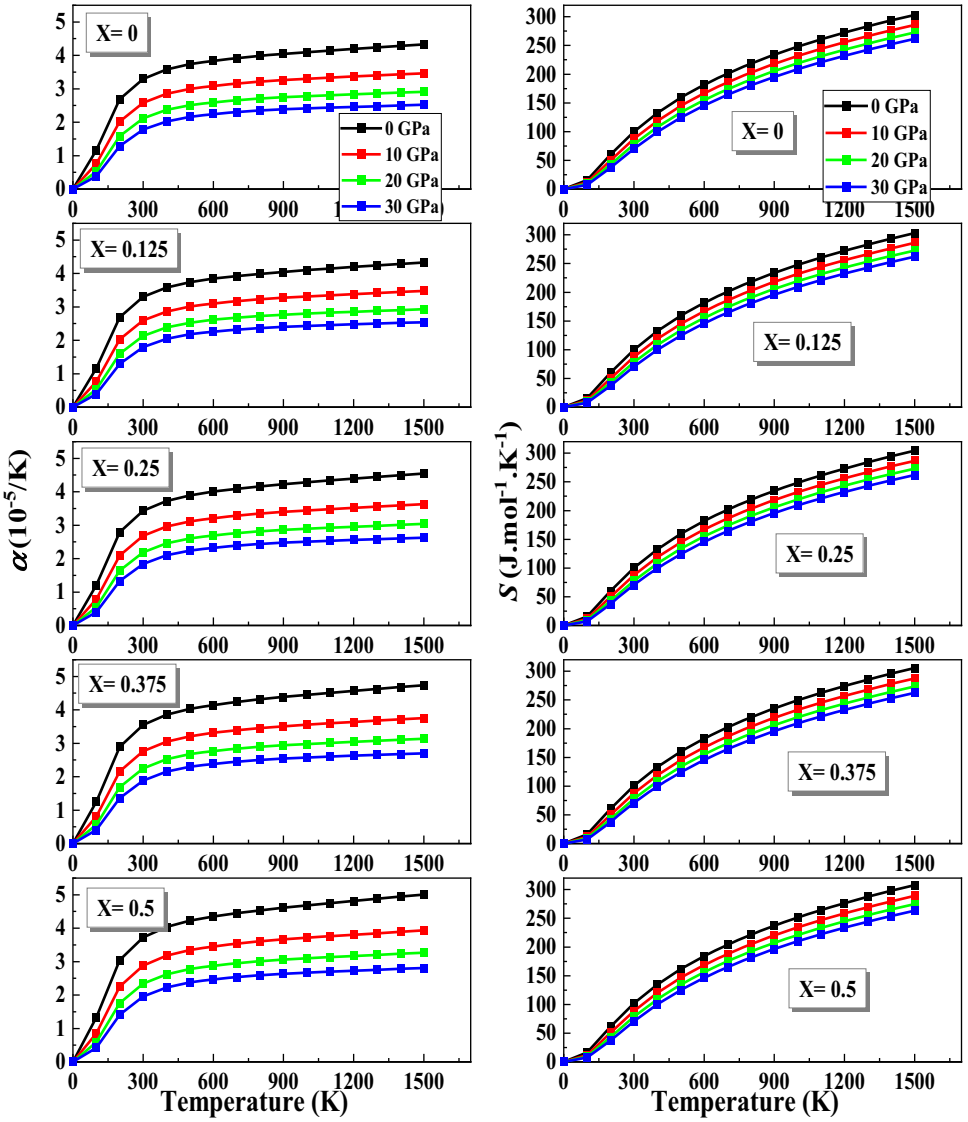

Fig. 12 Temperature dependence of the thermal expansion (α) and the entropy (S) of the $ZrSr_{1-x}Ru_xO_3$ at applied fixed hydrostatic pressures of 0, 10, 20, and 30 GPa

Table 3 Isochoric heat capacity (C_V in J mol^{-1} K^{-1}), the entropy (S in J mol^{-1} K^{-1}), lattice thermal conductivity (k_l, in W m^{-1} K^{-1}), the thermal expansion factor (α), Debye temperature(θ_D, in K), and Grüneisen parameter (γ, dimensionless) of $ZrSr_{1-x}Ru_xO_3$ calculated at 0 GPa and 300 K

x	C_V (J/mol·K)	S (J/mol·K)	θ_D (K)	γ	α (10^{-5}/K)	K_l (W·m^{-1}·K^{-1})
0.000	105.860	100.028	552.900	2.027	3.299	0.791
0.125	105.843	99.974	553.180	2.017	3.301	1.600
0.250	105.902	100.160	552.210	2.077	3.431	1.493
0.375	106.040	100.599	549.930	2.121	3.548	1.409
0.500	106.418	101.819	543.650	2.156	3.724	1.313

parameter is reduced with increasing Ru content according to Vegard's law, confirming ideal solid solution behavior; (2) the band gap of Sr(Zr, Ru)O_3 exhibits strong nonlinear bowing and is highly sensitive to the Ru concentration. It is transitioning from an insulating state ($SrZrO_3$, $E_g = 4.20$ eV) to a half-metallic phase at $x = 0.125$ and finally to a metallic state at $x = 0.5$, in agreement with virtual crystal approximation predictions; (3) by adding Ruthenium to $SrZrO_3$, it passes through three phases, where at Ru concentration of ($x = 0.125$), strontium zirconate changes from an insulator to a half-metallic. Then, at a Ru concentration of ($x = 0.5$), it turns into a metallic state; (4) the mixture of oxygen $2p$ states with the $4d-$t2g states of both Ru and Zr plays a significant role in the optical transitions in $SrZr_{1-x}Ru_xO_3$ perovskites. The $SrZr_{1-x}Ru_xO_3$ compound exhibits low coefficient of thermal expansion, and its lattice thermal conductivity is under 4.0 W m^{-1} K^{-1} at room temperature and 30 GPa.

These findings demonstrate that $SrZr_{1-x}Ru_xO_3$ is a versatile material with tunable electronic and magnetic properties, offering significant potential for use in spintronics, sustainable energy technologies, and optoelectronic devices. However, experimental

validation is critical to confirm these predictions and explore uncharted applications beyond conventional perovskite oxides. Future work should focus on synthesizing these alloys and probing their catalytic, photovoltaic, and magnetotransport properties.

4.1 Supplemental material

This supplemental material includes a comprehensive table containing the spin magnetic moment of a $(2 \times 2 \times 2)$ supercell of cubic $SrZr_{1-x}Ru_xO_3$. Additionally, it comprises a figure illustrating tolerance and octahedral factors at varying Ru concentrations, along with figures depicting the total and partial DOS, and optical properties at different Ru concentrations.

Supplementary Information The online version contains supplementary material available at https://doi.org/10.1140/epjp/s13360-025-06448-0.

Acknowledgements The corresponding author thanks Zarqa University—Jordan—for the financial support and the mandated facilities that were provided to complete this work.

Data Availability Statement The manuscript has data included as electronic supplementary material.

References

1. M. Khalid Hossain, S.M. Kamrul Hasan, M. Imran Hossain, R.C. Das, H.K. Bencherif, M.H. Rubel et al., A review of applications, prospects, and challenges of proton-conducting zirconates in electrochemical hydrogen devices. Nanomaterials **12**, 3581 (2022)
2. R. Terki, H. Feraoun, G. Bertrand, H. Aourag, Full potential calculation of structural, elastic and electronic properties of $BaZrO_3$ and $SrZrO_3$. Phys. Status Solidi **242**(5), 1054–1062 (2005)
3. C.J. Howard, H.T. Stokes, Group-theoretical analysis of octahedral tilting in perovskites. Acta Crystallogr. Sect. B. **54**(6), 782–789 (1998)
4. B.J. Kennedy, C.J. Howard, B.C. Chakoumakos, High-temperature phase transitions in $SrZrO_3$. Phys. Rev. B **59**(6), 4023 (1999)
5. S.S.A. Gillani, R. Ahmad, I. Zeba, R.M. Islah-u-din, M. Rafique et al., Structural stability of $SrZrO_3$ perovskite and improvement in electronic and optical properties by Ca and Ba doping for optoelectronic applications: a DFT approach. Philos. Mag. **99**(24), 3133–3145 (2019)
6. S. Sâad Essaoud, S.M. Al Azar, A.A. Mousa, R.S. Masharfe, Characterization of structural, dynamic, optoelectronic, thermodynamic, mechanical and thermoelectric properties of AMgF3 (A = K or Ag) fluoro-perovskites compounds. Phys. Scr. **98**(3), 035820 (2023)
7. N. Al Aqtash, S.M. Al-Azar, A.Y. Al-Reyahi, A. Mufleh, M. Maghrabi, S.S. Essaoud et al., First-principles calculations to investigate structural, mechanical, electronic, optical, and thermoelectric properties of novel cubic double Perovskites X2AgBiBr 6 (X=Li, Na, K, Rb, Cs) for optoelectronic devices. Mol. Simul. **2023**, 1–12 (2023)
8. S.S. Essaoud, S.M. Azar, A.A. Mousa, A.Y. Al-Reyahi, DFT-based investigation of electronic-structure, magnetic and thermoelectric properties of Dy2CoMnO6 double perovskite. Phys. Scr. **98**(7), 075930 (2023)
9. H.H. Huang, M. Ishigame, S. Shin, Protonic conduction in the single crystals of Y-doped $SrZrO_3$. Solid State Ionics **47**, 251–255 (1991)
10. T. Schober, Water vapor solubility and impedance of the high temperature. Solid State Ionics **145**, 319–324 (2001)
11. C. Shi, M. Morinaga, Doping effects on proton incorporation and conduction in $SrZrO_3$. J. Comput. Chem. **27**(1), 711–718 (2006)
12. T. Shimura, K. Esaka, H. Matsumoto, H. Iwahara, Protonic conduction in Rh-doped $AZrO_3$ (A = Ba, Sr and Ca). Solid State Ionics **149**, 237–246 (2002)
13. T. Yajima, H. Suzuki, T. Yogo, H. Iwahara, Protonic conduction in $SrZrO_3$-based oxides. Solid State Ionics **51**, 101–107 (1992)
14. N. Ito, H. Matsumoto, S. Okada, T. Ishihara, *Application F, Data P. Proton Conductor, Electrochemical Cell and Method of Manufacturing Proton Conductor*. USA; US 2010/0304229 A1 (2010), p. 1–16
15. B. De Caprariis, P. De Filippis, V. Palma, A. Petrullo, A. Ricca, C. Ruocco et al., Rh, Ru and Pt ternary perovskites type oxides BaZr(1–x)MexO_3 for methane dry reforming. Appl. Catal. A Gen. **517**, 47–55 (2016)
16. C. Ruocco, B. De Caprariis, V. Palma, A. Petrullo, A. Ricca, M. Scarsella et al., Methane dry reforming on Ru perovskites, $AZrRuO_3$: influence of preparation method and substitution of A cation with alkaline earth metals. J. CO2 Util. Util. **30**, 222–231 (2019)
17. Y. Okada, T. Kita, R. Tamaki, M. Yoshida, A. Pusch, O. Hess et al., Intermediate band solar cells: recent progress and future directions. Appl. Phys. Rev. **2**, 021302 (2015)
18. M.H. Cho, Y.S. Lee, Electronic structure and red emission of Mn-ion-doped $SrZrO_3$. J. Korean Phys. Soc. **64**(12), 1866–1871 (2014)
19. H. Zhang, X. Fu, S. Niu, Q. Xin, Synthesis and photoluminescence properties of Eu3+-doped $AZrO_3$ (A = Ca, Sr, Ba) perovskite. J. Alloys Compd. **459**(1–2), 103–106 (2008)
20. J. Huang, L. Zhou, Z. Wang, Y. Lan, Z. Tong, F. Gong et al., Photoluminescence properties of $SrZrO_3$:Eu3+ and $BaZrO_3$:Eu3+ phosphors with perovskite structure. J. Alloys Compd. **487**(1–2), 10–12 (2009)
21. T.V.B. Sheetal, R. Arora, K.S.P. Dayawati, Synthesis, structural and optical properties of $SrZrO_3$:Eu3+ phosphor. J. Rare Earths **32**(4), 293–297 (2014)
22. R.I. Eglitis, Ab initio calculations of $SrTiO_3$, $BaTiO_3$, $PbTiO_3$, $CaTiO_3$, $SrZrO_3$, $PbZrO_3$ and $BaZrO_3$ (001), (011) and (111) surfaces as well as F centers, polarons, KTN solid solutions and Nb impurities therein. Int. J. Mod. Phys. B **28**(17), 1430009 (2014)
23. S.S.A. Gillani, R. Ahmad, M. Rizwan, M. Rafique, G. Ullah, C.B. Cao et al., Effect of magnesium doping on band gap and optical properties of SrZrO3 perovskite: a first-principles study. Opt. Int. J. Light Electron. Opt. **191**, 132–138 (2019)
24. J.W. Park, K. Jung, M.K. Yang, J.K. Lee, D.Y. Kim, J.W. Park et al., Resistive switching characteristics and set-voltage dependence of low-resistance state in sputter-deposited $SrZrO_3$: Cr memory films. J. Appl. Phys. **99**, 124102 (2006)
25. L. Weston, A. Janotti, X.Y. Cui, B. Himmetoglu, C. Stampfl, W.C.G. Van De, Structural and electronic properties of $SrZrO_3$ and Sr(Ti, Zr)O_3 alloys. Phys. Rev. B **92**, 085201–085207 (2015)
26. S. Arya, A. Singh, A. Ahmed, B. Padha, A. Banotra, U. Parihar et al., Energizing tomorrow: the potential of light-driven supercapacitors in future applications. J. Energy Chem. **105**, 193–223 (2025)
27. A. Singh, S.S. Shah, A. Dubey, A. Ahmed, M. ud Din Rather, S.V. Ranganayakulu et al., Advancements in wearable energy storage devices via fabric-based flexible supercapacitors. J. Energy Storage **109**, 115183 (2025)
28. A. Ahmed, A. Singh, S. Arya, High performance Mn doped ZnO loaded rGO electrode and its practical application as an electrode for self-charging supercapacitor device. J. Energy Storage **105**, 114783 (2025)

29. A. Ahmed, S. Arora, S. Rasgotra, A. Dubey, A. Singh, R. Singh et al., Synthesis and characterization of low-density polyethylene (LDPE) bubble wrap-derived reduced graphene oxide for triboelectric nanogenerator electrodes. Mater. Sci. Eng. B **311**, 117828 (2025)
30. S. Dogra, A. Ahmed, A. Dubey, R. Singh, A. Singh, A.K. Sundramoorthy et al., Synthesis, characterization, and application of PVDF-PZT composite thin film separator for self-charging supercapacitors. Surfaces Interfaces **51**, 104593 (2024)
31. S. Arya, A. Sharma, A. Singh, A. Ahmed, A. Dubey, B. Padha et al., Review—energy and power requirements for wearable sensors. ECS Sens. Plus. **3**(2), 022601 (2024). https://doi.org/10.1149/2754-2726/ad54d2
32. P. Hohenberg, W. Kohn, Inhomogeneous electron gas. Phys. Rev. **136**(3B), B864–B871 (1964)
33. W. Kohn, L.J. Sham, Self-consistent equations including exchange and correlation effects. Phys. Rev. **140**, A1133 (1965)
34. P. Blaha, K. Schwarz, F. Tran, R. Laskowski, G.K.H. Madsen, L.D. Marks, WIEN2k: an APW+lo program for calculating the properties of solids. J. Chem. Phys. **152**(7), 074101 (2020)
35. A. Kokalj, Computer graphics and graphical user interfaces as tools in simulations of matter at the atomic scale. Comput. Mater. Sci. **28**(2), 155–168 (2003)
36. A. Otero-De-La-Roza, D. Abbasi-Pérez, V. Luaña, Gibbs: a new version of the quasiharmonic model code. II. Models for solid-state thermodynamics, features and implementation. Comput. Phys. Commun. **182**(10), 2232–2248 (2011)
37. F. Birch, Elasticity and constitution of the earth's interior. J. Geophys. Res. **57**(2), 60 (1952)
38. V.M. Von Goldschmidt, Die Gesetze der Krystallochemie. Perit. Dial. Int. **14**(21), 477–485 (1926)
39. C. Li, K.C.K. Soh, P. Wu, Formability of ABO_3 perovskites. J. Alloys Compd. **372**(1–2), 40–48 (2004)
40. N. Xu, H. Zhao, X. Zhou, W. Wei, X. Lu, W. Ding et al., Dependence of critical radius of the cubic perovskite ABO_3 oxides on the radius of A- and B-site cations. Int. J. Hydrogen Energy **35**(14), 7295–7301 (2010)
41. R.D. Shannon, Revised effective ionic radii and systematic studies of interatomie distances in halides and chaleogenides. Acta Cryst. **A32**, 751 (1976)
42. Z. Feng, H. Hu, S. Cui, C. Bai, First-principles study of optical properties of $SrZrO_3$ in cubic phase. Solid State Commun. **148**(9–10), 472–475 (2008)
43. E. Mete, R. Shaltaf, U. Srtio, Electronic and structural properties of a 4d perovskite : cubic phase of $SrZrO_3$. Phys. Rev. B **68**, 035119 (2003)
44. U. Qazi, S. Mehmood, Z. Ali, I. Khan, I. Ahmad, Electronic structure and magnetic properties of the perovskites $SrTMO_3$ (TM = Mn, Fe Co, Tc, Ru, Rh, Re, Os and Ir). Phys. B Phys. Condens. Matter. **2022**(624), 413361 (2021)
45. Q.J. Liu, Z.T. Liu, L.P. Feng, H. Tian, Mechanical, electronic, chemical bonding and optical properties of cubic $BaHfO_3$: first-principles calculations. Phys. B Condens. Matter. **405**(18), 4032–4039 (2010)
46. M. Yaseen, H. Shafiq, J. Iqbal, B.F. Misbah, A. Murtaza et al., Pressure induced electronic, optical and thermoelectric properties of cubic $SrZrO_3$: DFT investigation. Phys. B Condens. Matter. **612**(220), 412626 (2021)
47. Y.S. Lee, J.S. Lee, T.W. Noh, D.Y. Byun, K.S. Yoo, K. Yamaura et al., Systematic trends in the electronic structure parameters of the 4d transition-metal oxides $SrMO_3$ (M=Zr, Mo, Ru, and Rh). Phys. Rev. B Condens. Matter Mater. Phys. **67**(11), 113101 (2003)
48. A. Zhang, M. Lü, S. Wang, G. Zhou, S. Wang, Y. Zhou, Novel photoluminescence of $SrZrO_3$ nanocrystals synthesized through a facile combustion method. J. Alloys Compd. **433**(1–2), 7–11 (2007)
49. C. Ambrosch-Draxl, J.O. Sofo, Linear optical properties of solids within the full-potential linearized augmented planewave method. Comput. Phys. Commun. **175**(1), 1–14 (2006)
50. J. Sun, X.F. Zhou, Y.X. Fan, J. Chen, H.T. Wang, X. Guo et al., First-principles study of electronic structure and optical properties of heterodiamond BC2 N. Phys. Rev. B Condens. Matter. Mater. Phys. **73**(4), 1–10 (2006)
51. S.M. Al Azar, I. Al-zoubi, A. Mousa, R. Masharfe, E.K. Jaradat, Investigation of electronic, optical and thermoelectric properties of perovskite $BaTMO_3$ (TM = Zr, Hf): first principles calculations. J. Alloys Compd. **887**, 161361 (2021)
52. A.T. Petit, P.L. Dulong, Recherches sur Quelques Points Importants de la Théorie de la Chaleur. Ann. Chim. Phys. **10**, 395–413 (1819)
53. L.D. De, P. Richet, High-temperature heat capacity and thermal expansion of $SrTiO_3$ and $SrZrO_3$ perovskites. Phys. Rev. B **53**(6), 3013–3022 (1996)